Case Studies in Thermal Engineering 49 (2023) 103253

Contents lists available at ScienceDirect

Case Studies in Thermal Engineering

journal homepage: www.elsevier.com/locate/csite

Modification technique for a space manipulator Joint's thermal model parameters

Min Zhang [a,b,c], Chunlong Liu [a,c,*], Richa Hu [a,c], Hasiaoqier Han [a,b,c], Qingwen Wu [a,c]

[a] Changchun Institute of Optics, Fine Mechanics and Physics, Chinese Academy of Sciences, Changchun, 130033, China
[b] School of Materials Science and Optoelectronic Technology, University of Chinese Academy of Sciences, Beijing, 100049, China
[c] CAS Key Laboratory of On-orbit Manufacturing and Integration for Space Optics System, Changchun, 130033, China

ARTICLE INFO

Handling Editor: Dr Y Su

Keywords:
Space manipulator's joint
Thermal simulation analysis
Surrogate model
Optimal solution
Model updating

ABSTRACT

This study takes into account the multi-point thermal model's automatic adjustment mechanism. The combined heat balance test temperature is used as the genetic algorithm's optimization target value. To minimize time and resources when running simulations, a back propagation neural network-based surrogate model between temperature and parameters is used. The best parameter set is discovered when the thermal model is modified at high temperatures. The overall temperature distribution of the thermal model is significantly improved by the 50% decrease in the heat transfer coefficient X_1 of the joint body and the multi-layer insulation assembly, among others. The model's root-mean-square error before and after the adjustment is decreased from 4.51 °C to 0.95 °C. The best parameter set has been effectively contrasted and validated by reintroducing it into the low temperature environment. When the model is updated, the root-mean-square error drops from 2.73 °C to 1.09 °C. Following the model update, the joint temperature distribution is more in accord with the experimental findings, and all errors are within 2 °C. Therefore, the finite element thermal model of a space manipulator joint can be altered using a combination of back propagation neural network and genetic algorithm.

Nomenclature

Q_1 =	sum of three kinds of external heat flux absorbed by the joint surface of the manipulator (W)
Q_{sun} =	direct solar heat flux (W)
Q_{ref} =	Earth-reflected heat flux (W)
Q_{Eair} =	Earth infrared-radiation heat flux (W)
α_s =	solar absorption coefficient of the external joint surface
ε_h =	infrared hemisphere emissivity of the external articular surface
Φ_1 =	solar irradiation angle coefficient for the outer surface of the joint
Φ_2 =	Earth's albedo angle coefficient for the outer surface of the joint
Φ_3 =	Earth's irradiation angle coefficient for the outer surface of the joint
S =	solar constant (W/m^2)

* Corresponding author. Changchun Institute of Optics, Fine Mechanics and Physics, Chinese Academy of Sciences, Changchun, 130033, China.
E-mail address: 6033610432lcl@163.com (C. Liu).

https://doi.org/10.1016/j.csite.2023.103253
Received 11 March 2023; Received in revised form 18 June 2023; Accepted 2 July 2023
Available online 5 July 2023

E_r = Earth's albedo heat flux on the outer surface of the joint (W/m^2)
E_e = Earth's irradiated heat flux on the outer surface of the joint (W/m^2)
A_1 = effective heat transfer areas of the joint surface for solar irradiation (m^2)
A_2 = effective heat transfer areas of the joint surface for Earth's albedo (m^2)
A_3 = effective heat transfer areas of the joint surface for Earth's irradiation (m^2)
Q_2 = heat produced by the heat source inside the joint (W)
q_i = heat source inside the joint (W)
Q_3 = radiative heat transfer between the joint and external environment (W)
Q_4 = radiation heat transfer between the manipulator joint surface and the cabin body (W)
Q_5 = energy change generated by the joint itself (W)
m_k = mass of a joint component (kg)
c_k = specific heat capacity of a joint component (J/(kg·K))
$\frac{\partial T}{\partial \tau}$ = temperature change rate of a joint component (°C/s)
T = temperature of a characteristic part of the joint (°C)
f = functional relationship between the temperature of each characteristic part of the joint and relevant thermal design parameters
Φ_i = angle-of-view coefficient
A_i = effective heat transfer areas (m^2)
m_i = mass (kg)
c_i = specific heat capacity (J/(kg·K))
R_i = contact thermal resistance (K/W)
k_i = contact heat transfer coefficient (W/(m^2·°C))
X_1 = heat transfer coefficient between multilayer insulation material and body (W/(m^2·°C))
X_2 = contact heat transfer coefficient between side plate 1 of electric box and outside side plate 1 of electric box (W/(m^2·°C))
X_3 = contact heat transfer coefficient between electric box side plate 1 and electric box side plate 2 and 4 (W/(m^2·°C))
X_4 = contact heat transfer coefficient between side plate 1 and top plate of electric box (W/(m^2·°C))
X_5 = contact heat transfer coefficient between the bottom plate of the electric box and the inner plate of the side plate 1 of the electric box (W/(m^2·°C))
X_6 = contact heat transfer coefficient between the bottom plate of the electric box and the outer plate of the side plate 1 of the electric box (W/(m^2·°C))
X_7 = contact heat transfer coefficient between electric box side plate 1 and electric box top plate (W/(m^2·°C))
X_8 = contact heat transfer coefficient between handrail pad and joint shell (W/(m^2·°C))
X_9 = contact heat transfer coefficient between joint inner shell and joint end cap (W/(m^2·°C))
X_{10} = contact heat transfer coefficient between the joint inner shell and the joint shell (W/(m^2·°C))
X_{11} = contact heat transfer coefficient between the joint shell and the bottom of the electric box (W/(m^2·°C))
X_{12} = contact heat transfer coefficient of joint shell and female connection (W/(m^2·°C))
X_{13} = contact heat transfer coefficient between joint shell and ring gasket (W/(m^2·°C))
X_{14} = contact heat transfer coefficient between male connection and insulation mat (W/(m^2·°C))
X_{15} = contact heat transfer coefficient between female connection and insulation mat (W/(m^2·°C))
Y = objective function (°C)
xia = the lower limits of thermal design parameters (W/(m^2·°C))
xib = the upper limits of thermal design parameters (W/(m^2·°C))
z = the number of joint temperature measurement points
TP_i = predicted temperature at the i^{th} measurement point (°C)
TA_i = test temperature at the i^{th} measurement point (°C)
F = fitness function (°C^{-1})
T_1 = electricity box + X measuring point temperature (°C)
T_2 = electricity box -Y measuring point temperature (°C)
T_3 = electricity box + Y measuring point temperature (°C)
T_4 = joint shell -Y + Z measuring point temperature (°C)
T_5 = joint shell -Y-Z measuring point temperature (°C)
T_6 = joint shell -Z measuring point temperature (°C)
T_7 = joint shell -X + Y measuring point temperature (°C)

Abbreviations

BPNN = back-propagation neural network
GA = genetic algorithm
RMSE = root-mean-square error

1. Introduction

Space manipulator has emerged as a popular study issue in aerospace due to the rising demand for on-orbit service of space devices [1]. A space manipulator is essential for on-orbit activities like spacecraft construction and maintenance. It is the essential component of a spacecraft's in-orbit system [2]. However, when it operates in orbit, the space manipulator is entirely situated in the chilly, dark extravehicular environment. Its internal heat source consumes a lot of power and its motion posture is changeable. It is particularly negatively impacted by external heat flux, which causes significant temperature differences at various locations and significant temperature fluctuations at various times. A suitable thermal design must be used in order to maintain a reasonable temperature range [3]. This necessitates ongoing research on finite element thermal simulations and precise temperature field predictions for each machine as the space manipulator operates in orbit [4]. Consequently, it is imperative to have a precise finite element thermal model. Typically, the initial thermal model's temperature distribution is not very precise [5]. Because there will be some variation between the calculated results and the experimental data during the process of creating the thermal model of aeronautical products for thermal analysis. Numerous academics have conducted a great deal of related study [6–8]. This needs to continuously update the thermal model by changing the thermal design parameters. W. B. Qin enhanced the update technology of the spacecraft thermal network model based on the formulation of the thermal grid combination equation of parameter node group. This fixed the issue where there aren't enough temperature monitoring points for the model correction to work during thermal testing [9]. When Q. Li wanted to adjust the thermal analysis model parameters for the carbon dioxide detector in layers, he used the Monte Carlo approach to determine how

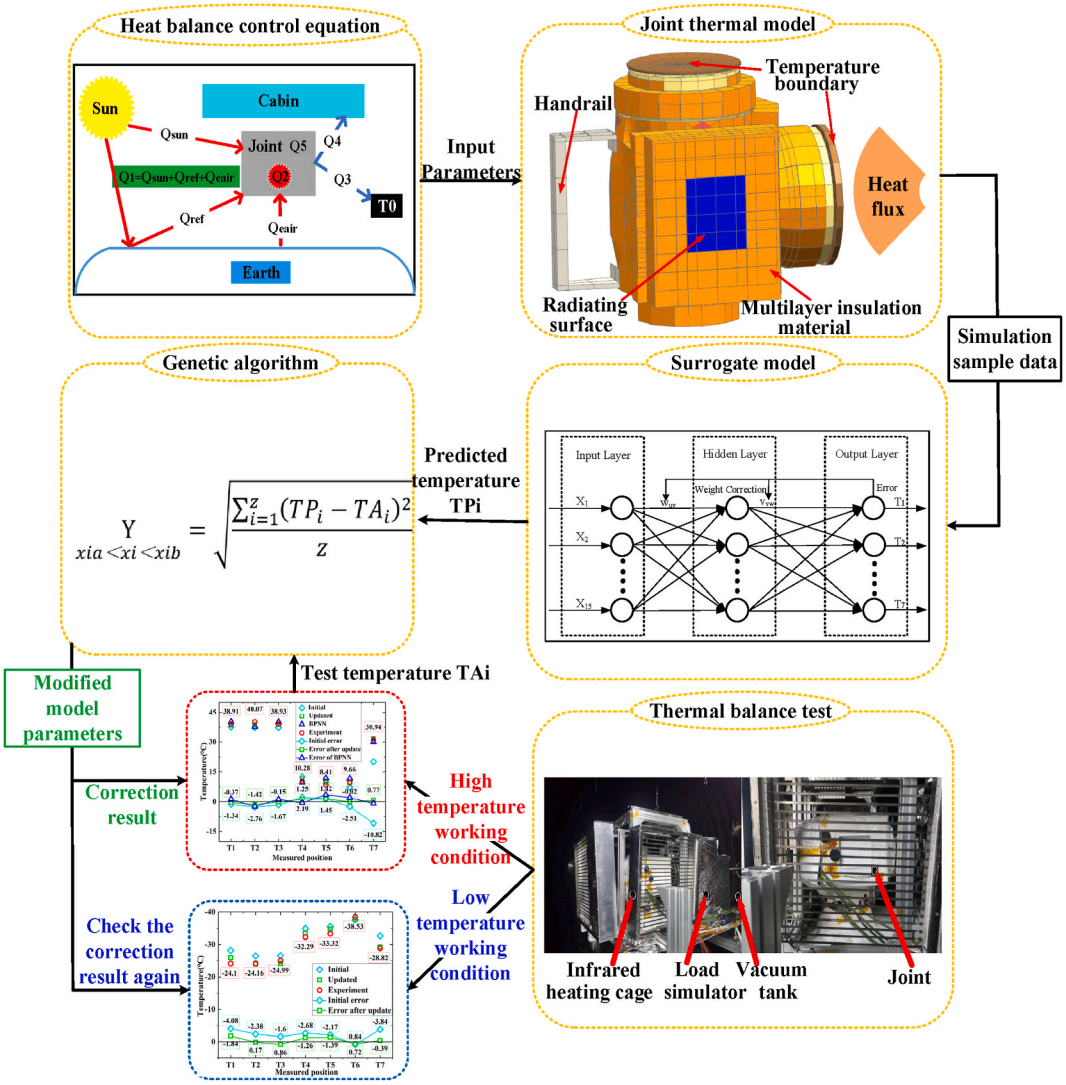

Fig. 1. Modification of a space manipulator's joint thermal model.

sensitive they were. The majority of temperature discrepancies were decreased by an order of magnitude after the correction [10].

The majority of professionals in spacecraft thermal management still adjust the parameters by hand using engineering knowledge and theoretical analysis [11]. In addition to taking a lot of time, this method cannot ensure that the changed thermal model is the best. For the joint of the main space manipulator components, a multi-point thermal model update approach is therefore taken into consideration. This approach can successfully verify the correction impact between a number of measuring locations, in addition to meeting the industry's desire for automatic correction of thermal models. The genetic algorithm (GA), first suggested by Holland [12] in 1975, is an algorithm that seeks out the best answer globally. This algorithm has the benefit over previous optimization algorithms [13–15] in that it does not require prior consideration of pertinent domain information. Additionally, as a population is assessed throughout each iteration as a whole, the interaction between the input parameters can be efficiently taken into account. This approach is currently being used in numerous engineering disciplines [16–18]. Szenasi, S. employed GA to research the inverse heat conduction problem against the backdrop of parameter identification and control parameter optimization of the thermal system [19]. Anglada, E. employed GA to automatically correlate the equipment during a thermal test with the spacecraft's mathematical thermal model. Improvements have been made to spacecraft thermal control design and verification [20].

Thus, the primary objective of this study is to incorporate GA into the process of thermal model parameter modification. By using the joint thermal balance test temperature as the optimization goal value, temperature prediction accuracy is increased. The temperature of important measuring locations in various positions is compared to one another in the joint thermal model correction to increase the method's dependability. The objective function specifies the root-mean-square error (RMSE) of the anticipated temperature and test temperature of measuring sites at various places. This reduces the likelihood of producing a single variable. A surrogate model based on Back Propagation Neural Network (BPNN) is used in this paper to analyze the relationship between the temperature of multiple measuring points and the parameters of a joint thermal model, saving time and resources by replacing simulation calculations with it. BPNN [21] can adapt to this complicated and dynamic nonlinear system more successfully than other algorithms [22–24].

2. Study on parameter modification of thermal model

A space manipulator's joint thermal model parameters can be modified in four steps, as shown in Fig. 1. (a) To start, the thermal design parameters for efficient modeling are chosen in accordance with the joint's thermal balancing control equation. The parameters' suitable customizable range is established. This part is stated in Section 2.1. (b) The BPNN technique is then used to build a surrogate model between the parameters and the projected temperature TP_i. This part is included in Section 2.2.1. (c) The test value TA_i is the temperature distribution data from the thermal balance test performed at a high temperature, and it is used to adjust the joint thermal model's parameters. This section focuses on Sections 2.2.2, 2.2.3, and 3. (d) The adjustment effect of the joint thermal model parameters is then once more examined using the results of the thermal balancing test at low temperatures. This part is described in Section 4. For changing the thermal model of aerospace products, this strategy has significant directing implications.

2.1. Selection of thermal model parameters

Internal heat source and space environment are two factors that affect the joint temperature of a space manipulator. According to Fig. 2, the thermal balance equation [25] of a space manipulator joint is given.

$$Q_1 + Q_2 = Q_3 + Q_4 + Q_5. \tag{1}$$

$$Q_1 = Q_{sun} + Q_{ref} + Q_{Eair} = \alpha_s \Phi_1 S A_1 + \alpha_s \Phi_2 E_r A_2 + \varepsilon_h \Phi_3 E_e A_3. \tag{2}$$

$$Q_2 = \sum q_i. \tag{3}$$

$$Q_5 = \sum \left(m_k c_k \frac{\partial T}{\partial \tau} \right). \tag{4}$$

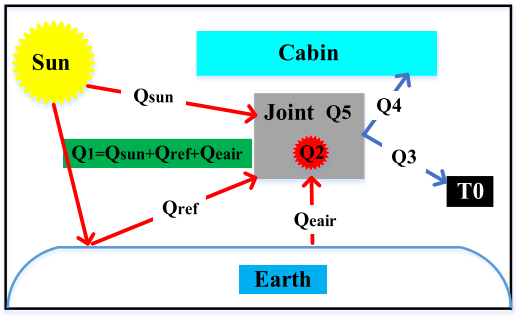

Fig. 2. Schematic of heat exchange at the joint of a space manipulator.

A joint's response to external heat flux, or Q_1, includes three types of external heat flux from space: direct sunlight, or $\alpha_s\Phi_1 SA_1$, Earth-reflected, or $\alpha_s\Phi_2 E_r A_2$, and Earth infrared-radiation, or $\varepsilon_h\Phi_3 E_e A_3$; Q_2 represents the heat that the heat source produces; Q_3 represents the radiative heat transfer between the joint and external environment; Q_4 represents the radiation heat transfer between the manipulator joint surface and the cabin body; Q_5 represents the energy change generated by the joint itself; q_i is the heat source; α_s is solar absorption coefficient of the external joint surface; ε_h is infrared hemisphere emissivity of the external joint surface; Φ_i is the angle coefficient between two objects; A_i is the effective area between two heat transfer objects; m_k is the mass of a joint component; c_k is the heat capacity of a joint component; $\frac{\partial T}{\partial \tau}$ is the temperature change rate of a joint component.

Equations (1)–(4) indicate that the power consumption of the internal components of the joint, the external heat flux, and the heat transfer capacity of the joint surface are important factors affecting the temperature of the joint shell of the space manipulator. It is difficult to obtain an analytical expression for the relationship between the temperature of each characteristic point of the joint and each thermal design parameter. To accurately analyze the effects of thermal design parameters on the temperature of each characteristic part of the joint, the temperature of each characteristic part of the joint is expressed using the inverse solution of the thermal balance equation and various influencing factors [25]:

$$T = f(\Phi_i, A_i, \alpha_s, \varepsilon_h, k_i, m_i, R_i, c_i, \cdots), \tag{5}$$

where T is the temperature of a characteristic part of the joint, °C, and f represents the functional relationship between the temperature of each characteristic part of the joint and relevant thermal design parameters. The contact thermal resistance between the various components of the joint is denoted R_i and the contact heat transfer coefficient is denoted k_i. Φ_i is the angle-of-view coefficient.

In the above function, some design parameters, such as Φ_i and A_i, cannot be arbitrarily changed because they are limited by the structure size, working conditions, and space environment of the joint. Some thermal design parameters, such as α_s and ε_h, are fixed by the selection of the thermal control materials themselves and cannot be changed arbitrarily. Some design parameters, such as k_i and R_i, can be adjusted and selected according to need in their effective ranges. On the basis of the aforementioned parameter analysis, the significant heat transmission path and the intricate contact condition between surfaces are taken into consideration. Table 1 lists the 15 thermal design parameters that will be chosen. The heat transfer coefficient between the joint body and the multi-layer insulating component is designated by the symbol X_1. In the simulation computation, X_1 often changes in the range of 0.01–2 W/(m^2·°C) due to varied multi-layer implementation states, according to the literature study [26] and practical experience summary. The contact heat transfer coefficient (X_2–X_{15}) between two components depends on the gap medium, contact load, and other external parameters in addition to the roughness of the contact surface. Previous experimental observations reveal that X_2–X_{15} typically fluctuates between 100 and 3000 W/(m^2·°C). As a result, these modifiable thermal design factors dictate the temperature T at each distinct site of the joint. By setting different boundary conditions, such as the contact heat transfer coefficient, the corresponding temperature distribution surrogate model is trained.

2.2. BPNN-GA thermal model parameter correction method

2.2.1. BPNN agent model

The BPNN comprises an input layer, hidden layer, and output layer and can be used to simulate the nonlinear relationship between input and output [27]. In the training process, the input signals of the neural network are nonlinearly transformed to calculate the desired output. Finally, the difference (error) between the desired output and actual output is obtained and fed back to the hidden layer to obtain the ideal model. The BPNN used in this article is shown in Fig. 3. As observed in the picture, the input group ranges from X_1 to X_{15}. The output group is T_1–T_7, and the number of hidden layer nodes is fixed at 30 in accordance with the modeling expertise of BPNN.

The steps of the BPNN model's training procedure [28] are shown in Fig. 4. (a) The distribution of values for the aforementioned 15

Table 1
Thermal design parameters used to establish the BPNN model.

Symbol	Parameter	Value range(W/(m^2·°C))
X_1	Heat transfer coefficient between multilayer insulation material and body	0.01–2
X_2	Contact heat transfer coefficient between side plate 1 of electric box and outside side plate 1 of electric box	100–3000
X_3	Contact heat transfer coefficient between electric box side plate 1 and electric box side plate 2 and 4	100–3000
X_4	Contact heat transfer coefficient between side plate 1 and top plate of electric box	100–3000
X_5	Contact heat transfer coefficient between the bottom plate of the electric box and the inner plate of the side plate 1 of the electric box	100–3000
X_6	Contact heat transfer coefficient between the bottom plate of the electric box and the outer plate of the side plate 1 of the electric box	100–3000
X_7	Contact heat transfer coefficient between electric box side plate 1 and electric box top plate	100–3000
X_8	Contact heat transfer coefficient between handrail pad and joint shell	100–3000
X_9	Contact heat transfer coefficient between joint inner shell and joint end cap	100–3000
X_{10}	Contact heat transfer coefficient between the joint inner shell and the joint shell	100–3000
X_{11}	Contact heat transfer coefficient between the joint shell and the bottom of the electric box	100–3000
X_{12}	Contact heat transfer coefficient of joint shell and female connection	100–3000
X_{13}	Contact heat transfer coefficient between joint shell and ring gasket	100–3000
X_{14}	Contact heat transfer coefficient between male connection and insulation mat	100–3000
X_{15}	Contact heat transfer coefficient between female connection and insulation mat	100–3000

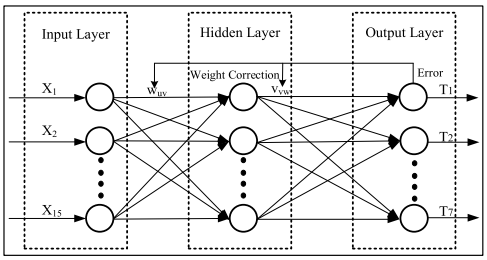

Fig. 3. Structure of the BPNN.

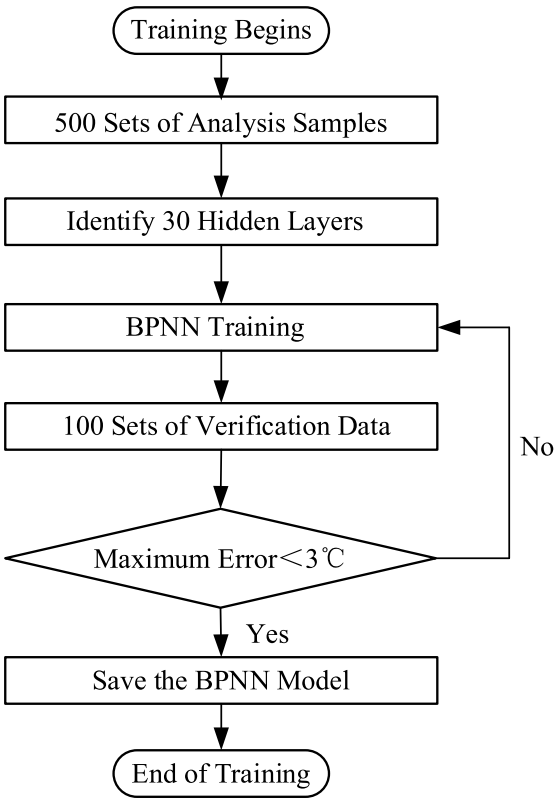

Fig. 4. BPNN model training process.

thermal design parameters is uniform. Table 2 displays the sampling results of 500 sets of random data samples of design parameters. (b) 500 sets of sample data are substituted into the finite element model to be modified. The temperature of each characteristic point corresponding to 500 groups of thermal design parameters is obtained by finite element model simulation calculation. Boundary conditions and thermal control state are high temperature operating circumstances at the moment. Table 3 provides a description of

Table 2
Partial parameter data used to preliminarily establish the BPNN surrogate model.

Num.	X_1(W/(m^2·°C))	X_2 (W/(m^2·°C))	…	X_{15} (W/(m^2·°C))	T_1 (°C)	T_2 (°C)	…	T_6 (°C)	T_7(°C)
1	1.63	2108.34	…	1527.80	16.93	15.74	…	−7.42	6.2
2	1.81	1714.34	…	2114.76	18.5	16.58	…	−8.79	3.83
3	0.26	1249.91	…	2920.93	32.41	32.19	…	6.79	19.54
4	1.83	278.61	…	1050.49	18.89	17.99	…	−8.999	3.05
…	…	…	…	…	…	…	…	…	…
497	1.49	1053.56	…	501.94	19.25	18.02	…	−7.13	7.36
498	0.79	1996.05	…	1805.81	24.75	23.61	…	−1.47	11.61
499	1.31	2272.48	…	1161.85	19.56	18.18	…	−5.39	8.04
500	0.35	1791.24	…	2439.60	30.62	30.22	…	4.72	17.42

Table 3
Low- and high-temperature conditions.

Condition	High temperature condition	Low temperature condition
Multilayer outer film properties	Final	Initial
Heat dissipation surface white paint properties	Final	Initial
Handrail surface properties	Final	Initial
Joint tooling boundary temperature	−30 °C	+50 °C
The heat flux	The maximum solar constant is 1412 W/m^2	0
Internal heat source working condition	8 h working mode	Don't work
Active temperature control measures	Don't start	Start

the boundary conditions and analytical parameters for high temperature and low temperature circumstances. During the orbit, the manipulator's joint's stance is not fixed. As a result, other potential low temperature scenarios can be covered by the calculation based on the extreme case where the cooling surface is cold and black. Other potential high temperature scenarios can be covered by the extreme case where the cooling surface always faces the sun. (c) The BPNN model is trained using 500 sets of analysis samples. (d) The difference (error) between the actual value and the anticipated value is then tested using 100 sets of calibration data. (e) The training is scheduled to end when the error is less than 3.0 °C based on engineering experience.

A joint has complicated and erratic overall structural features. A joint's overall temperature distribution can be correctly characterized by seven measuring points, which are chosen (see Fig. 9). In order to create seven BPNN models that satisfy the training conditions from seven measuring points, repeated training is required. This is equivalent to the corresponding temperatures of T_1 through T_7. Figs. 5 and 6 display temperature errors for several test samples as determined by a finite element model and seven BPNN surrogate models. The joint electric box is where the measuring points T_1–T_3 are all set. On the joint shell, the measuring points T_4 through T_7 are all organized. The errors of the seven BPNN models are all fewer than 3.0 °C, according to observation. As a result, the nonlinear functional relationship between the joint thermal design parameters and the temperature of seven measuring points can be accurately represented by seven BPNN surrogate models. Additionally, seven BPNN models' results for forecasted temperature can be compared to one another during the parameter modification. This improves the accuracy of the joint thermal model modification.

2.2.2. GA optimization

GA is an algorithm that is based on the optimization principle of finding the best option. The process of model updating is also an optimization problem in essence. In this paper, the GA is used to search for the optimal parameter group within reasonable ranges of the thermal design parameters. This set of parameters minimizes the objective function (i.e., the difference between BPNN prediction results and heat balance test results). The objective function is [29]

$$\underset{xia<xi<xib}{Y} = \sqrt{\frac{\sum_{i=1}^{z}(TP_i - TA_i)^2}{z}}, \tag{6}$$

where Y is the objective function; xia and xib are respectively the lower and upper limits of thermal design parameters; z is the number of joint temperature measurement points; TP_i is the predicted temperature at the i^{th} measurement point; and TA_i is the test temperature

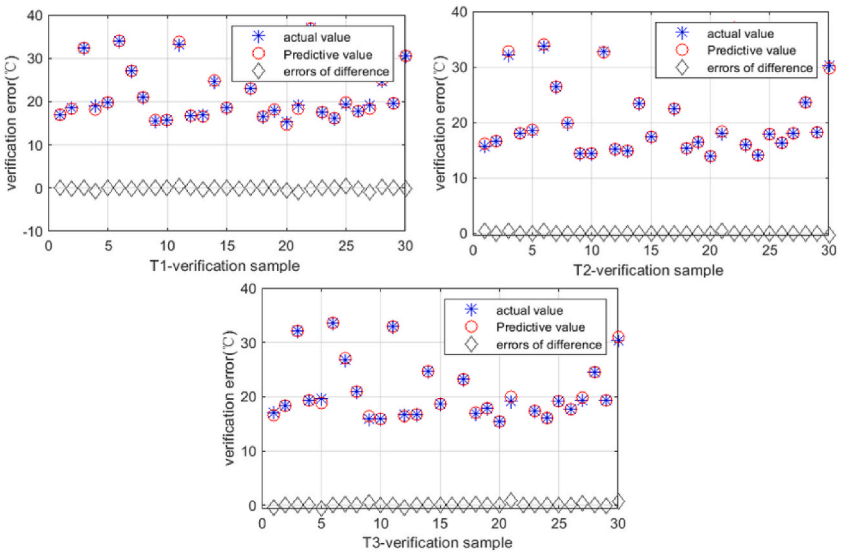

Fig. 5. Comparison of results between simulation model and surrogate model of measuring points T_1–T_3 of electric box.

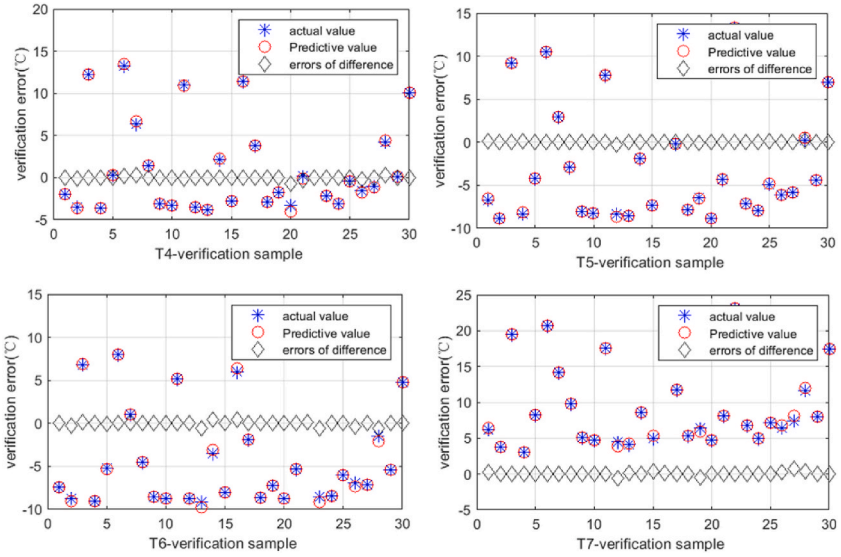

Fig. 6. Comparison of results between simulation model and surrogate model of measuring points T_4–T_7 of joint shell.

at the i^{th} measurement point.

Fig. 7 depicts the GA optimization process, and the steps are as follows: (a) Determine the fitness function. Assume that the fitness function F is the reciprocal of the objective function Y+1. (b) Genetic manipulation. The roulette approach is utilized in this study to

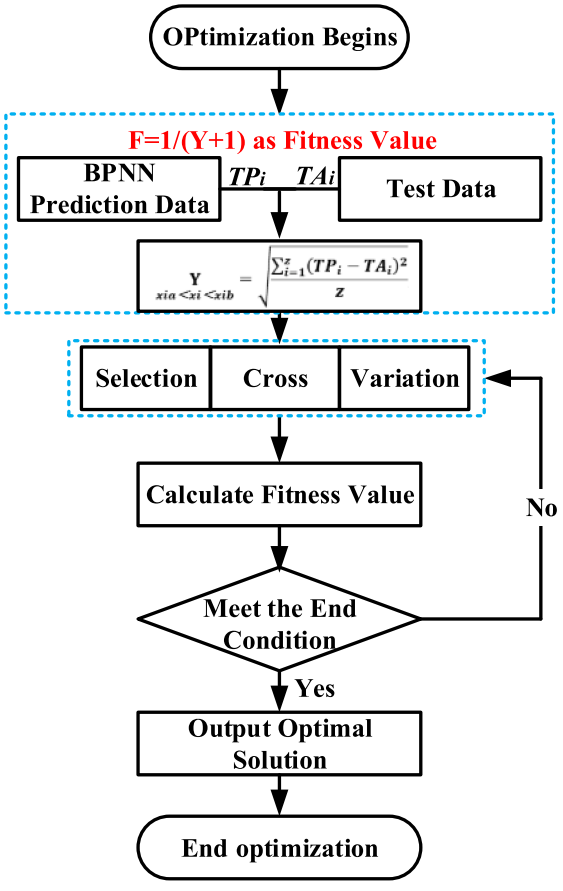

Fig. 7. Optimization process of GA.

determine the individual selection probability based on the individual fitness value. Uniform mutation and single-point crossover are used to carry out the genetic operation. (c) Evolutionary individuals. The individual with the best fitness in the function is acquired after random mutation and crossover operations. The operation is complete because this person is the best remedy for the issue. If not, proceed to step (b).

$$F = \frac{1}{Y+1}, \tag{7}$$

2.2.3. Thermal balance test

The thermal design of the joint of the space manipulator is shown in Fig. 8. The exterior of the joints is coated in a multilayer insulation material that isolates the effects of the external heat flux and cold black space. The heat produced as the joint moves dissipates through the heat dissipation surface and a complicated heat dissipation path to the cold, dark environment. In order to counteract heat loss, a heating component is simultaneously glued into a crucial joint location. The thermal balance test is conducted in accordance with the thermal design of the joint. The thermal balance test device and platform are shown in Fig. 8. To replicate the cold, dark, and vacuum of space, a joint is placed in a space environment simulator. To imitate the external heat flux to the joint, an infrared heating cage is utilized. The layout of temperature measurement points is depicted in Fig. 9 for the thermocouple, which is used to measure a joint's temperature at various locations.

3. Modification of thermal model parameters at high temperature

3.1. Optimal set of input parameters for thermal model modification under high temperature conditions

The finite element model of the space manipulator joint is established in the finite element simulation program in accordance with the structural model of the space manipulator joint. The model has 197 thermal couplings and 5675 two-dimensional shell pieces, as depicted in Fig. 8. Before the finite element thermal model of joint is modified, the initial temperature simulated by the thermal model under high temperature and the test temperature under the same thermal balance test are shown in Table 4. Table 4 shows that there are different degrees of error between the initial simulation value and the test values for T_1–T_7. The temperature difference between T_2, T_5, and T_6 is about 2 °C. The temperature difference of T_7 is about 10.82 °C. The research suggests that the location of contact between the joint shell and the electric box shell may be the cause of the large temperature differential of T_7. The adjustability of the parameters close to them is imprecise due to the measurement's difficulty. The initial value is empirically estimated. Additionally, the electric box itself provides a significant amount of heat for prolonged operation. The temperature difference between the simulation and the experiment could result from this.

Following the parameter optimization described in Section 2.2.2, Table 5 displays the ideal input parameter group and percentage change. X_1 changes through optimization by 50% to 0.08 W/(m^2·°C). This is so because X_1—the coefficient of heat transmission between the joint body and the multilayer thermal insulation materials—is used in the thermal simulation study. It contains inescapable flaws and is significantly influenced by the thermal control implementation method. The 0.08 W/(m^2·°C) after X_1 correction is still within the acceptable range according to empirical research, though. X_6, X_7, X_{13}, and X_{15} change considerably in the model update, with X_6 and X_7 being 4.5–4.8 times their original values. This is because X_2–X_{15} is the contact heat transfer coefficient, which depends on the contact load, gap medium and other external factors, especially the roughness of the contact surface. These large changes result from the increase in contact pressure due to the fastening installation of side plate 1 of the electric box with the top plate and bottom plate of the electric box. Meanwhile, the contact heat transfer coefficients X_{13} and X_{15} are 2.1–3.7 times their original values because the roughness of the contact surface between the male and the boundary and the roughness of the contact surface between the female connection and the boundary are very low.

3.2. Temperature field of the modified thermal model under high temperature conditions

To evaluate the results of model optimization, revert to the finite element model using the ideal parameter set from Section 3.1. Table 6 and Fig. 10 display the improved model's temperature distribution. The initial simulated temperature of the joint is lower than that in the thermal balance test before the parameters are modified. The multi-layer coating process is primarily to blame for the temperature increases that have occurred as a result of changing the parameters at each measuring point. Although thermal insulation

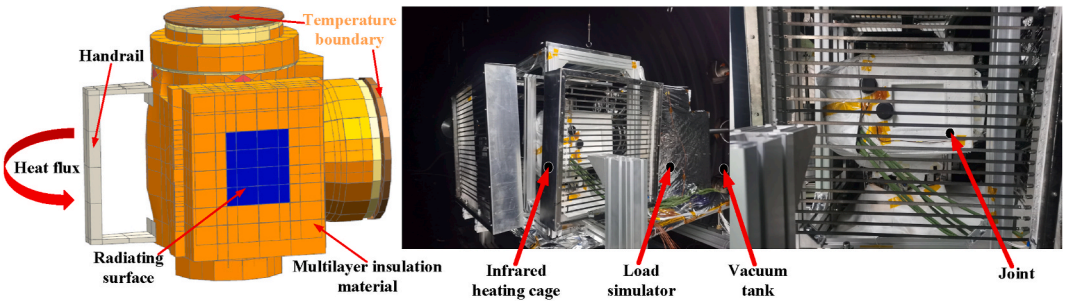

Fig. 8. Finite element model and thermal balance test platform of a space manipulator joint.

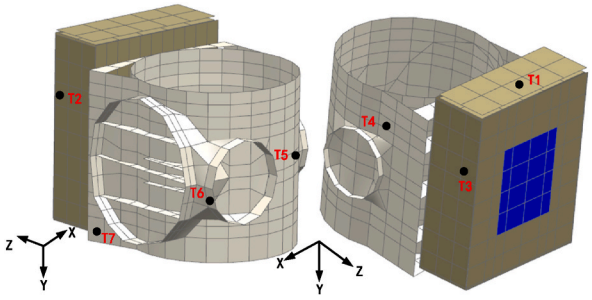

Fig. 9. Locations of temperature measurements.

Table 4
Comparison of initial simulation temperature of the finite element model and thermal balance test temperature under a high-temperature condition.

Thermocouple	T_1	T_2	T_3	T_4	T_5	T_6	T_7
Experiment (°C)	38.91	40.07	38.93	10.28	8.41	9.66	30.94
Simulation (°C)	37.57	37.31	37.26	12.47	9.86	7.15	20.12
Initial error(%)	3.44	6.88	4.28	−21.30	−17.24	25.98	34.97

Table 5
Update of the thermal design parameters.

Parameters	Unit	Initial value	Lower bound	Upper bound	Optimized value	Percent change (%)
X_1	W/(m^2·°C)	0.16	0.01	2	0.08	−50
X_2	W/(m^2·°C)	300	300	2000	383.46	27.81
X_3	W/(m^2·°C)	300	300	2000	333.65	11.21
X_4	W/(m^2·°C)	300	300	2000	426.22	42.07
X_5	W/(m^2·°C)	300	300	2000	514.84	71.61
X_6	W/(m^2·°C)	300	300	2000	1756.59	485.52
X_7	W/(m^2·°C)	300	300	2000	1652.90	450.96
X_8	W/(m^2·°C)	300	300	2000	323.39	7.79
X_9	W/(m^2·°C)	300	300	2000	355.33	18.44
X_{10}	W/(m^2·°C)	300	300	2000	333.84	11.28
X_{11}	W/(m^2·°C)	300	300	2000	543.41	81.13
X_{12}	W/(m^2·°C)	300	300	2000	374.80	24.93
X_{13}	W/(m^2·°C)	300	300	2000	1409.39	369.79
X_{14}	W/(m^2·°C)	300	300	2000	388.20	29.39
X_{15}	W/(m^2·°C)	300	300	2000	944.26	214.75

Table 6
Temperature comparison at seven measuring points under the high-temperature condition.

	Initial(°C)	Updated(°C)	Experiment(°C)	Initial error(%)	Error after update(%)
T_1	37.57	38.54	38.91	3.44	0.95
T_2	37.31	38.65	40.07	6.88	3.54
T_3	37.26	38.78	38.93	4.28	0.38
T_4	12.47	11.53	10.28	−21.30	−12.15
T_5	9.86	9.83	8.41	−17.24	−16.88
T_6	7.15	9.64	9.66	25.98	0.20
T_7	20.12	31.71	30.94	34.97	−2.48

materials have been applied to the joint surface, the status of multi-layer thermal implementation technology has a significant impact on each measuring point's temperature. It is impossible to anticipate the multilayer and joint body's heat transfer coefficient at some overlapped places and at the boundary between multilayer coated and uncoated regions. Consequently, the ideal finite element thermal model cannot be directly and correctly simulated. Therefore, the heat transfer coefficient between the multi-layer and joint body decreases with the update of parameter X_1 at high temperature. The joint's simulated temperature increases. T_6 and T_7 in particular undergo significant alteration, with T_7 rising by nearly 10 °C. The adjusted X_1 and the thermal characteristics close to the measurement point can be used to evaluate the clearly higher temperature at the measuring point T_7. X_5, X_6, X_7, X_{11} and X_{15} are all contact heat transfer coefficients close to the measuring site T_7, and they all exhibit observable variations before and after adjustment. The temperature of T_7 definitely rises through heat conduction between the electric box and the female connector as a result of the higher contact heat transfer coefficient. Each distinctive point's temperature fluctuates clearly, as can be observed. The RMSE of the

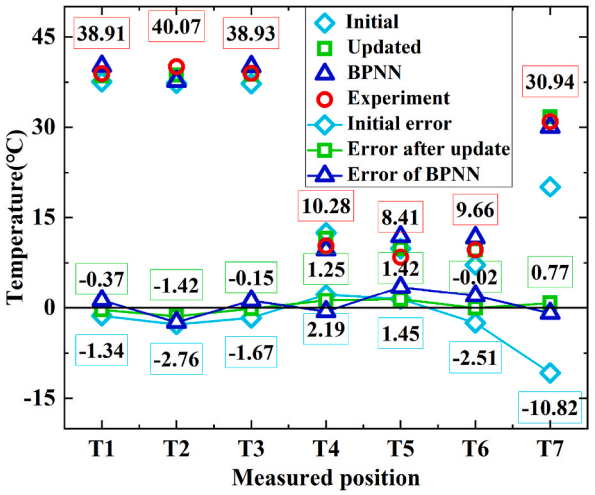

Fig. 10. Temperature comparison at seven measuring points under the high-temperature condition.

model before and after updating is decreased from 4.51 °C to 0.95 °C at high temperatures. It can be said that the updated model's temperature is closer to the experimental data. The largest temperature difference between the BPNN model and the finite element model is also 2.02 °C, further demonstrating the BPNN model's accuracy.

4. Verification and discussion of model modification

The same set of thermal design parameters that were optimized for high-temperature conditions are added to the low-temperature finite element thermal model in order to further evaluate Section 3.1. Table 3 lists the high temperature and low temperature circumstances. Thus, it is possible to determine the updated thermal model's temperature at low temperatures. The thermal model temperature and test temperature at low temperature are shown in Table 7 and Fig. 11. The initial simulated temperature of a joint before updating the parameters is typically lower than that in the thermal balance test performed in low temperature settings. The temperature at each measuring location has risen to varied degrees as a result of the parameter updates. The multilayer coating process's X_1 parameter decrease has an impact on it as well. The measuring stations T_1, T_2, T_3 and T_7 in particular all experience an increase in temperature of roughly 2 °C before and after the thermal model update. Measurement sites T_1 through T_3 are all located on the joint electrical box, while T_7 is a measurement point on the joint shell that is situated next to the electrical box and the female connection. The reason is that the electric box's contact heat transfer coefficients, X_4, X_5, X_6, X_7 and X_{11}, are all evident parameters. The contact heat transfer coefficient between the female connector and the joint shell is parameter X_{15}. The temperature of the measurement point visibly rises due to their increase and the impact of active heating measures initiated at low temperatures. The RMSE of the simulation temperature and test temperature decreased from 2.73 °C to 1.09 °C thanks to the optimization of the thermal model. It may be said that the adjusted model's temperature is more in line with the low-temperature experimental data. So, a comparison and verification of the improved finite element thermal model has been successfully completed.

Both high and low temperatures can be handled by the improved joint thermal model. The improved joint thermal model's anticipated temperature and the thermal test temperature differ by less than 2 °C under the identical operating conditions. The comparison analysis mentioned above demonstrates the proposed method's advantage. This offers other thermal models in orbit a very solid technological foundation for temperature prediction.

This paper further verifies the efficiency of metamodel modification. It took 1 h, 42 min, and 12 s for a computer to solve the thermal simulation model of the joint under the high-temperature condition using finite element software and took the same computer 19 min and 54 s to iteratively optimize the parameters of the joint model and solve the output temperature of the parameters. The efficiency of parameter updating using the surrogate model is about 5.14 times that of the traditional method. Additionally, optimizing models in finite element software requires researchers to have a rich engineering experience and an in-depth understanding of the joint

Table 7
Temperature comparison at seven measuring points under the low-temperature condition.

	Initial(°C)	Updated(°C)	Experiment(°C)	Initial error(%)	Error after update(%)
T_1	−28.18	−25.94	−24.1	−16.92	−7.63
T_2	−26.54	−23.99	−24.16	−9.85	0.70
T_3	−26.59	−24.13	−24.99	−6.40	3.44
T_4	−34.97	−33.55	−32.29	−8.29	−3.90
T_5	−35.49	−34.71	−33.32	−6.51	−4.17
T_6	−37.69	−37.81	−38.53	2.18	1.86
T_7	−32.66	−29.21	−28.82	−13.32	−1.35

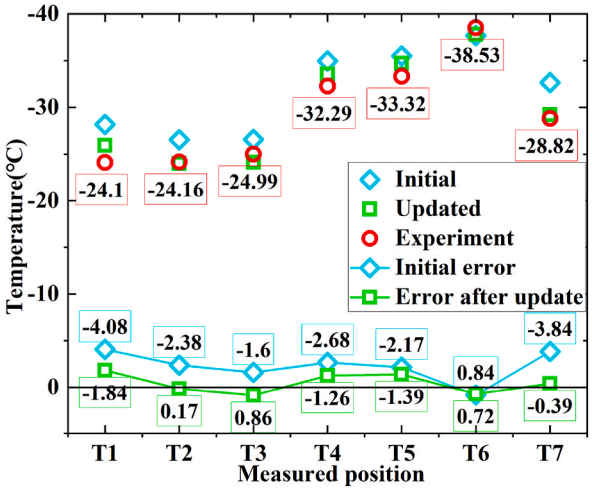

Fig. 11. Temperature comparison at seven measuring points under the low-temperature condition.

thermal model, which have unpredictable associated time costs.

5. Conclusion

The primary objective of this study is to alter a space manipulator joint's finite element thermal model by merging BPNN and GA technologies. This increases temperature prediction accuracy and is crucial to the accomplishment of upcoming space missions.

(1) The introduction of GA into the thermal model parameter correction procedure is the primary objective of this study. As the optimization goal value, the joint thermal balance test temperature is used. A multi-point thermal model update method is taken into account. This technique allows for automatic thermal model correction in industry. It also takes into account the fact that the effect of adjustment between a number of thermal model measurement points can be successfully tested against one another. This paper also uses a surrogate model based on BPNN to reduce the time and resources required for simulation calculation. The joint thermal model's parameters and the temperature at various monitoring places serve as the surrogate model. The thermal model of aerospace products can be modified using this technology, which has substantial guiding implications.

(2) The primary finding of this study is that, when thermal model parameters are modified, X_1 represents the multi-layer and joint body's heat transfer coefficient. The thermal model's overall temperature distribution is effectively improved by its 50% adjustment. The temperature of local joint characteristic points is visibly adjusted by other contact heat transfer factors. At high temperature, the RMSE of the model before and after the entire update is decreased from 4.51 °C to 0.95 °C. The RMSE of the model before and after the entire update is decreased from 2.73 °C to 1.09 °C at low temperatures. This increases the precision of temperature forecasting. Following the model update, the joint temperature distribution is more in accord with the experimental findings, and all errors are within 2 °C. As a result, the space manipulator's finite element thermal model can be modified using BPNN and GA together.

(3) A joint thermal model's updated findings are promising. However, there is still a lot of work that can be done more effectively. The following recommendations for further work are made due to the research's limitations. (a) The combined BPNN thermal model's parameter selection is based on the thermal control equation and experience. Both sensitivity analysis and systematic parameter sorting are absent from this. Future study can take the sensitivity of thermal design elements into account. Additionally, it has some reference expertise for spaceflight product thermal design. (b) The temperature adjustment is limited by the number of measuring points in the thermal test and is focused on seven distinguishing spots on the joint. The prediction accuracy of the location other than the seven measurement sites must be looked into in order to examine the overall performance of the improved joint thermal model. (c) This study only takes changing working conditions into account when modifying and validating the joint thermal model. Future studies can concentrate on improving the algorithm's use in additional spacecraft products.

Funding

This research did not receive any specific grant from funding agencies in the public, commercial, or not-for-profit sectors.

Author statement

Author 1 (First Author): Min Zhang: Conceptualization, Formal Analysis, Investigation, Methodology, Software, Visualization, Writing - Original Draft, Writing - Review & Editing; Author 2 (Corresponding Author): Chunlong Liu: Conceptualization, Funding Acquisition, Methodology, Supervision, Validation, Writing - Review & Editing; Author 3: Richa Hua: Methodology, Supervision,

Validation; Author 4: Hasiaoqier Han: Resources, Supervision; Author 5: Qingwen Wu: Funding Acquisition, Project Administration, Supervision, Validation.

Declaration of competing interest

The authors declare that they have no known competing financial interests or personal relationships that could have appeared to influence the work reported in this paper.

Data availability

Data will be made available on request.

Acknowledgment

We thank Liwen Bianji (Edanz) (www.liwenbianji.cn) for editing the language of a draft of this manuscript.

References

[1] Y. Fu, Q. Jia, G. Chen, T. Li, Motion capability optimization of space manipulators with free-swinging joint failure, J. Aero. Eng. 36 (2023), https://doi.org/10.1061/(ASCE)AS.1943-5525.0001502.
[2] A. Flores-Abad, O. Ma, K. Pham, S. Ulrich, A review of space robotics technologies for on-orbit servicing, Prog. Aero. Sci. 68 (2014) 1–26, https://doi.org/10.1016/j.paerosci.2014.03.002.
[3] C.L. Bertagne, T.J. Cognata, R.B. Sheth, C.E. Dinsmore, D.J. Hartl, Testing and analysis of a morphing radiator concept for thermal control of crewed space vehicles, Appl. Therm. Eng. 124 (2017) 986–1002, https://doi.org/10.1016/j.applthermaleng.2017.06.062.
[4] F. QingLin, W. YanBo, L. ShuXuan, L. JianMing, D. Tao, L. Jiayu, A thermal vacuum environment adaptive design method and test for a space manipulator joint, in: 2015 International Conference on Fluid Power and Mechatronics (FPM), 2015, https://doi.org/10.1109/fpm.2015.7337221.
[5] C. Zheng, H. Zhao, Z. Zhou, Z. Geng, Z. Cui, Investigation on thermal model updating of Alpha Magnetic Spectrometer in orbit based on Kriging meta-modeling, Nucl. Instrum. Methods Phys. Res. Sect. A Accel. Spectrom. Detect. Assoc. Equip. 1031 (2022), 166581, https://doi.org/10.1016/j.nima.2022.166581.
[6] A. Abbas, I.E. Sarris, M. Ashraf, K. Ghachem, N. Hnaien, B.M. Alshammari, The effects of reduced gravity and radiative heat transfer on the magnetohydrodynamic flow past a non-rotating stationary sphere surrounded by a porous medium, Symmetry 15 (2023) 806, https://doi.org/10.3390/sym15040806.
[7] A. Abbas, M. Ashraf, I.E. Sarris, K. Ghachem, T. Labidi, L. Kolsi, et al., Numerical simulation of the effects of reduced gravity, radiation and magnetic field on heat transfer past a solid sphere using finite difference method, Symmetry 15 (2023) 772, https://doi.org/10.3390/sym15030772.
[8] M. Ashraf, A. Khan, A. Abbas, A. Hussanan, K. Ghachem, C. Maatki, et al., Finite difference method to evaluate the characteristics of optically dense gray nanofluid heat transfer around the surface of a sphere and in the plume region, Mathematics 11 (2023) 908, https://doi.org/10.3390/math11040908.
[9] W.B. Qin, H.E. Cheng, Correction Technique of Spacecraft Thermal Network Model on the Basis of Node Group Combined Method, vol. 6, Shanghai Jiaotong Daxue Xuebao/Journal of Shanghai Jiaotong University, 2011, pp. 856–860. https://xuebao.sjtu.edu.cn/EN/Y2011/V45/I06/856.
[10] Q. Li, L. Chen, Correction for transient thermal analysis model of Carbon Dioxide detector, Chin. Space Sci. Technol. 37 (2017) 44–52, https://doi.org/10.16708/j.cnki.1000-758X.2017.0004.
[11] N.P. Semena, The use of scale models in ground tests reproducing heat transfer in space, Thermophys. Aeromechanics 21 (2014) 45–55, https://doi.org/10.1134/s0869864314010053.
[12] M. Asim, A.A. Abd El-Latif, Intelligent computational methods for multi-unmanned aerial vehicle-enabled autonomous mobile edge computing systems, ISA (Instrum. Soc. Am.) Trans. 132 (2023) 5–15, https://doi.org/10.1016/j.isatra.2021.11.021.
[13] Z. Cheng, H. Song, D. Zheng, M. Zhou, K. Sun, Hybrid firefly algorithm with a new mechanism of gender distinguishing for global optimization, Expert Systems with Applications 224 (2023) 120027. https://doi.org/10.1016/j.eswa.2023.120027.
[14] P.G. Dhawale, V.K. Kamboj, S.K. Bath, A Levy flight based strategy to improve the exploitation capability of arithmetic optimization algorithm for engineering global optimization problems, Trans. Emerg. Telecommun. Technol. 34 (2023), https://doi.org/10.1002/ett.4739.
[15] L. Deng, S. Liu, A novel hybrid grasshopper optimization algorithm for numerical and engineering optimization problems, Neural Process. Lett. (2023), https://doi.org/10.1007/s11063-023-11230-3.
[16] A.S. Ghiduk, A. Alharbi, Generating of test data by harmony search against genetic algorithms, Int. Autom. Soft Comput. 36 (2023) 647–665, https://doi.org/10.32604/iasc.2023.031865.
[17] X. Wu, Y. Yang, Y. Sun, Y. Xie, X. Song, B. Huang, Dynamic regional splitting planning of remote sensing satellite swarm using parallel genetic PSO algorithm, Acta Astronaut. 204 (2023) 531–551, https://doi.org/10.1016/j.actaastro.2022.09.020.
[18] R. Szabo, R.-S. Ricman, A genetic algorithm-controlled solar tracker robot with increased precision due to evolution, Machines 11 (2023) 430, https://doi.org/10.3390/machines11040430.
[19] S. Szenasi, I. Felde, Configuring genetic algorithm to solve the inverse heat conduction problem, in: 2017 IEEE 15th International Symposium on Applied Machine Intelligence and Informatics (Sami), 2017, https://doi.org/10.1109/sami.2017.7880340.
[20] E. Anglada, I. Garmendia, Correlation of thermal mathematical models for thermal control of space vehicles by means of genetic algorithms, Acta Astronaut. 108 (2015) 1–17, https://doi.org/10.1016/j.actaastro.2014.11.042.
[21] X. Wang, H. Zhu, Active disturbance rejection control of bearingless permanent magnet synchronous motor based on genetic algorithm and neural network parameters dynamic adjustment method, Electronics 12 (2023) 1455, https://doi.org/10.3390/electronics12061455.
[22] Z. Chen, Research on internet security situation awareness prediction technology based on improved RBF neural network algorithm, J. Comput. Cogn. Eng. 1 (2022) 103–108, https://doi.org/10.47852/bonviewJCCE149145205514.
[23] J. Khan, E. Lee, K. Kim, A Higher Prediction Accuracy–Based Alpha–Beta Filter Algorithm Using the Feedforward Artificial Neural Network, CAAI Transactions on Intelligence Technology, 2022, https://doi.org/10.1049/cit2.12148.
[24] T. Tyagi, S. Kumar, A.K. Malik, V. Vashisth, A novel neuro-optimization technique for inventory models in manufacturing sectors, J. Comput. Cogn. Eng. (2022), https://doi.org/10.47852/bonviewJCCE2202184.
[25] C.J. Savage, Thermal control of spacecraft, Spacecraft Syst. Eng. (2011) 357–394, https://doi.org/10.1002/9781119971009.ch11.
[26] Z. Yuan, L. Chen, H. Han, L. Ren, S. Liu, R. Wang, Optimal design of thermal control system for space optical remote sensor based on NSGA-II and opto-mechanical-thermal integration analysis, Case Stud. Therm. Eng. 43 (2023), 102813, https://doi.org/10.1016/j.csite.2023.102813.
[27] Y. Ai, X. Shao, P. Jiang, P. Li, Y. Liu, W. Liu, Welded joints integrity analysis and optimization for fiber laser welding of dissimilar materials, Opt Laser. Eng. 86 (2016) 62–74, https://doi.org/10.1016/j.optlaseng.2016.05.011.
[28] Z.H. Zhu, Z.F. Ye, Y. Tang, Nondestructive identification for gender of chicken eggs based on Ga-BPNN with double hidden layers, J. Appl. Poultry Res. 30 (2021), 100203, https://doi.org/10.1016/j.japr.2021.100203.
[29] W.-J. Xu, L.-J. He, G.-Y. Zhu, Many-objective flow shop scheduling optimisation with genetic algorithm based on fuzzy sets, Int. J. Prod. Res. 59 (2019) 702–726, https://doi.org/10.1080/00207543.2019.1705418.